Atmospheric Density Estimation in Very Low Earth Orbit Based on Nanosatellite Measurement Data Using Machine Learning

Tomoki SAKAI[a,*], Yusuke TAKAHASHI[b]

[a]*Graduate School of Engineering, Hokkaido University, Kita 13 Nishi 8, Kita-ku, Sapporo, 060-8628, Hokkaido, Japan*
[b]*Faculty of Engineering, Hokkaido University, Kita 13 Nishi 8, Kita-ku, Sapporo, 060-8628, Hokkaido, Japan*

Abstract

The atmospheric density in the very low Earth orbit (VLEO), the lower region of the thermosphere is a critical factor for satellite missions on prediction of orbit and lifetime. However, accurately determining atmospheric density remains challenging owing to difficulties in acquiring data within the VLEO. The re-Entry satellite with Gossamer aeroshell and GPS/Iridium (EGG) nanosatellite mission, conducted in 2017, obtained sparse coordinate data through the iridium network and Global Navigation Satellite System (GNSS). Using these data, we developed a methodology based on machine learning and special perturbations to estimate atmospheric density. The originally obtained atmospheric density predicted by NRLMSISE-00 was corrected during trajectory reproduction from GNSS data by special perturbation. The prediction performance of the method was validated using the generated trajectory data. Subsequently, we estimated the density at altitudes of approximately 200 km, particularly in the lower region of the VLEO. Density values that accurately reproduced trajectories of the EGG were 0.5 to 0.64 times greater than that predicted by the NRLMSISE-00 model. This methodology is effective for measuring atmospheric density in the lower VLEO region using GNSS data from low-cost and high-frequency nanosatellite missions. By increasing the availability of accurate atmospheric density data, this methodology enhances our understanding of the atmosphere in the VLEO.

Keywords: Thermospheric density, Gaussian process regression, Bayesian optimization, Satellite trajectory

1. Introduction

The very Low Earth Orbit (VLEO), which is at an altitude range of 100–400 km, the lower region of the thermosphere, is poised to become a hub for future satellite operations. This range is lower than the altitudes at which Earth observation satellites have traditionally operated. Therefore, the spatial accuracy increases, and the sensor transmission power decreases in this altitude range. The VLEO has been the primary field for nanosatellites. Numerous nanosatellite missions have been carried out in the VLEO, often facilitated by deployment opportunities, such as the Japanese Experiment Module (JEM) Small Satellite Orbital Deployer (J-SSOD). This system releases nanosatellites from the JEM Kibo airlock aboard the International Space Station (ISS) at an altitude of 400 km.

*Corresponding Author
Email address: `tomozoelms1999@eis.hokudai.ac.jp` (Tomoki SAKAI)

Atmospheric density is an important factor in the VLEO. Satellites are decelerated by the aerodynamic force proportional to the atmospheric mass density (hereafter, density), which is expressed by the following equation:

$$\boldsymbol{F}_{aero} = -\frac{1}{2}\rho C_D A|\boldsymbol{v}|^2 \frac{\boldsymbol{v}}{|\boldsymbol{v}|} \tag{1}$$

where ρ is the density, and C_D , A, and $\boldsymbol{v}$ are the drag coefficient, front projected area, and velocity of the satellite, respectively. The density at the VLEO is significantly higher than that at higher altitudes. Consequently, the aerodynamic force described in Eq. 1 is magnified and has a considerable impact on the orbit and function of the satellite. Therefore, accurate prediction of density is essential for effectively utilizing this region. However, this task is challenging. First, observations in this region are difficult. Satellites that collect measurement data cannot remain in this region for extended periods owing to the large aerodynamic forces, and observation balloons cannot ascend to this altitude. Second, the density in this region changes rapidly and drastically owing to solar activity and geomagnetic conditions, which are measured respectively as $F10.7$, representing the solar radio flux at 10.7 cm wavelength, and the Ap index, a daily average indicator of geomagnetic activity.

Considerable efforts have been made to estimate the thermospheric (90–600 km) density [1][2]. The existing methods are those based on orbit derivations [3] [4], accelerometers [5][6][7], Global Navigation Satellite System (GNSS) data [8][9], Broglio drag balance instruments [10][11], neutral mass spectrometers [12][13], ultraviolet remote sensing [14], pressure gauge [15], incoherent scatter radar [16][17], and atmosphere occultation [18][19]. Various empirical models based on measurement data have also been constructed: the MSIS series (MSIS [20][21], MSIS-83 [22], MSIS-86 [12], [23], NRIMSISE-00 [24], and NRLMSISE 2.0 [25]), DTM series ([26], DTM94 [27], DTM-2000 [28], and DTM-2013 [29]), and Jacchia series ([30], Jacchia-70 [31], Jacchia-71 [32],HASDM [33], and JB2006 [34]).

Orbit-derived density or density estimated from accelerometers is used as global density data. Density derived from orbits is estimated based on satellite drag or orbital perturbation, primarily through variations in the orbit's semi-major axis. This method is highly versatile as it uses tracking data from satellites such as the two-line orbital element (TLE). Two methods are used to obtain the orbit-derived density: Global perturbation (GP) and special perturbation (SP). GP is used to analytically calculate orbits from the satellite TLE data using an orbit propagator, such as SGP4 [35], whereas SP calculates the orbits by evolving the satellite's equations of motion over time. These methods were compared and a method was developed to calculate the density from the difference between the GP orbit and observed orbit [3]. The density predicted by the Jacchia-70 model was corrected using SP and fitting orbital elements and ballistic coefficients using satellite-tracking data [4]. However, the density derived this way is typically averaged over a certain period of time. Hence, it may not capture rapid or short-term variations in atmospheric density, particularly in dynamic regions like the very low Earth orbit (VLEO). This could lead to less accurate predictions for satellite operations that require real-time or precise density information. Accelerometers provide density measurements with high temporal resolution; however, they are expensive and only a limited number of satellites have been equipped with them. Hence, the spatial coverage and historical extent of these measurements are less than that of the density measurements derived from orbits. Most of these density data came from satellites that orbit at altitudes of 400 km or higher for extended periods. Density data in the VLEO are limited because satellites in this range cannot remain in orbit for long periods. Hence, empirical models do not always accurately evaluate the VLEO density. Increasing the accuracy of atmospheric density measurements, particularly in the lower VLEO region, at an altitude of approximately 200 km, is crucial for enhancing our understanding of the atmosphere in VLEO. Therefore, a new and effective methodology for obtaining density data for VLEO is necessary.

Currently, many low earth orbit satellites are equipped with high-precision GNSS receivers and obtain high-temporal data. These data can be used to estimate the density by differentiating them and extracting the acceleration due to aerodynamic force [9][8]. Particularly, GNSS data from nanosatellites can be used to acquire density data in the VLEO, potentially increasing the quantity of available data. However, these nanosatellites typically have severe limitations in terms of budget, weight, and battery capacity. Therefore, data from such satellites may not always be readily accessible for density estimation.

The nanosatellite re-Entry satellite with the Gossamer aeroshell and GPS/Iridium (EGG), which departed from the ISS in 2017, obtained GNSS data in the VLEO. Figs. 1 and 2 show the concept of the EGG mission and its GNSS positioning data [36]. The horizontal axis of the GNSS data shows the number of days since the beginning of the mission, that is, the release from the ISS. The primary objectives of this flight demonstration were to (1) deploy an inflatable aeroshell in the VLEO, (2) achieve orbital decay by the aerodynamic force acting on the inflatable aeroshell, and (3) establish telemetry and command systems using the Iridium satellite network [37] in the VLEO. All communications with the EGG were via the Iridium satellite communication, eliminating the need for ground antennas. The EGG was released from the ISS on January 16, 2017; 27 days later, its membrane aeroshell was deployed in orbit by commands sent from the ground. The aeroshell deployment increased the EGG's front projected area and the aerodynamic force, which decelerated the EGG and collapsed its orbit. It thus gradually descended. The altitude data in Fig. 2 (c) depict this situation. In addition to the GNSS data, different types of data (e.g., temperature) were acquired via the Iridium satellite communications during the mission. However, they were intermittent, with intervals of tens to thousands of seconds, owing to the sub-optimal communication conditions.

Takahashi et al. performed trajectory reconstruction from the data using Gaussian process regression (GPR) [38] as the basis for the density estimation [36]. This method is effective when an input data set is sparse or complex. They showed that the position can be reconstructed from intermittent data; however, the accuracy of the velocity reconstruction is insufficient. Therefore, the methodology of utilizing GNSS introduced in [9] and [8] cannot be used with these data. Hence, after the trajectory reconstruction, they estimated the velocity of the EGG by fitting the trajectory using SP and Bayesian optimization (BO) [39] methods. They optimized the components of the initial velocity vector and found that these values were consistent with the altitude of

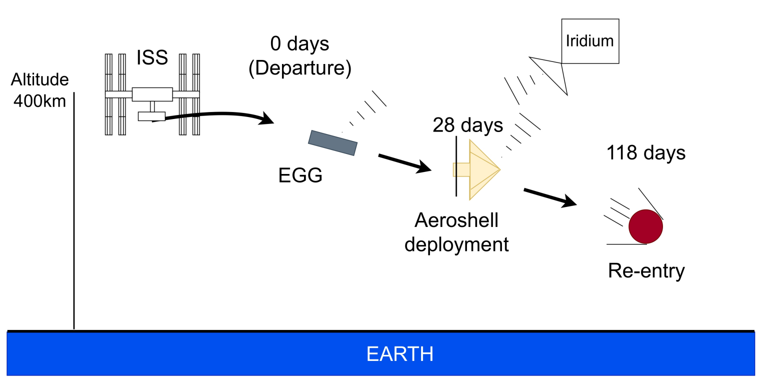

Figure 1: Concept of the EGG mission

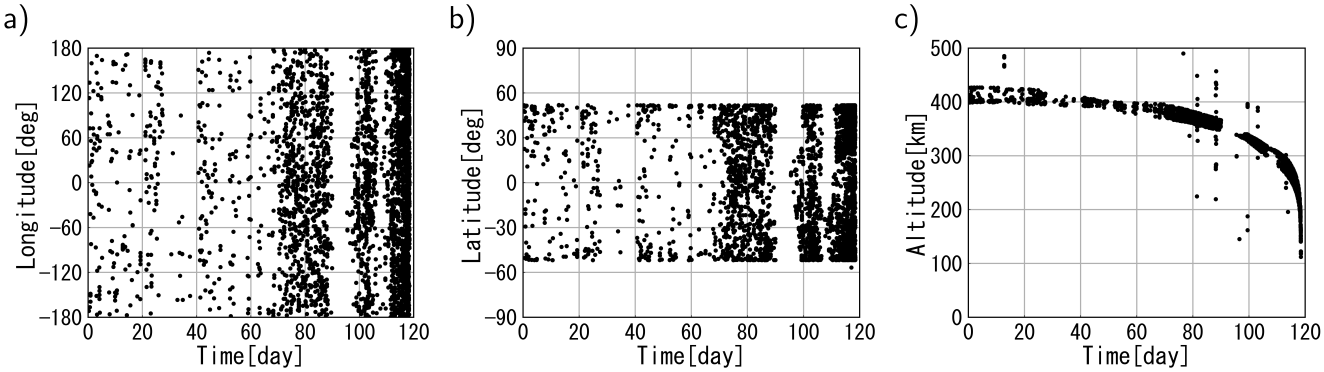

Figure 2: GNSS positioning data obtained by EGG

the reconstructed trajectory. In other words, they estimated the velocity that was not precisely obtained by the EGG from the intermittent GNSS data. The BO method was chosen because it could efficiently attain an optimal solution at a low computational cost, particularly when dealing with complex objective functions that vary across many input parameters. Its advantage lies in avoiding the pitfalls of local optimum solution. However, the density value was not optimized because its effect on the trajectory (altitude) was too small. The altitude of the GNSS data was approximately 330 km. By incorporating GNSS data from lower altitudes, where density has a greater impact, and integrating density values into the optimization parameters, it becomes feasible to estimate the density experienced by the EGG. In short, the orbit-derived density can be obtained from the nanosatellite's intermittent GNSS data.

If a methodology for estimating the density from the EGG data can be established, it can be applied to other nanosatellites. This technique will then provide more observations of the density in the VLEO, effectively filling the gap of missing mass density data in this region. This study aims to develop a methodology that can estimate density using intermittent GNSS data from nanosatellites and apply it to the EGG data. We used GNSS data from an altitude of approximately 200 km, which is a lower VLEO region.

In Section 2, we describe the density estimation methodology. Section 3 presents reconstructed trajectories from the EGG GNSS data. In Section 4, the validation of our methodology is described. The results of the application of the EGG data are presented in Section 5. Finally, Section 6 concludes the study.

2. Methodology

The concept of the density estimation methodology developed in this study is shown in Fig. 3. The basic idea is to reproduce a reconstructed trajectory (blue line) based on the measured GNSS data (black point), obtained by a nanosatellite using SP. GPR is used to reconstruct the trajectory. Among the input parameters of the SP, the components of the initial velocity vector and density are estimated using BO and grid search. The results (red line) are considered valid if the reconstructed trajectory is successfully reproduced. In other words, the density estimation in this study is an inverse problem of determining the appropriate input parameters based on the trajectory data derived from actual measurements and the SP output data.

This section describes the components of the methodology.

2.1. Trajectory reconstruction using Gaussian process regression

GPR is a regression method that does not require detailed assumptions on the basis functions and is easy to handle with few hyperparameters. It can be easily applied to complex and varying data using a small number of measurement points. We used this method because the GNSS data obtained by EGG was sparse owing to the characteristics of the Iridium satellite communications. In GPR, given a set of N input–output pairs $X = (\boldsymbol{x}_1, ..., \boldsymbol{x}_N)$ and $\boldsymbol{y} = (\boldsymbol{y}_1, ..., \boldsymbol{y}_N)$ as training data D, the probability distribution of the output $\boldsymbol{y}_*$ for a new input $\boldsymbol{x}_*$ is predicted as follows:

$$p(\boldsymbol{y}_*|\boldsymbol{x}_*, D) = (\boldsymbol{k}_*^T K^{-1}\boldsymbol{y}, k_{**} - \boldsymbol{k}_*^T K^{-1}\boldsymbol{k}_*). \tag{2}$$

Here, $\boldsymbol{k}_*$ is the vector of the kernel function k, defined as $\boldsymbol{k}_* = (k(\boldsymbol{x}_*, \boldsymbol{x}_1), k(\boldsymbol{x}_*, \boldsymbol{x}_2), ..., k(\boldsymbol{x}_*, \boldsymbol{x}_N))$. Furthermore, $k_{**} = k(\boldsymbol{x}_*, \boldsymbol{x}_*)$. K is the covariance function of X, defined as follows:

$$K = \begin{pmatrix} k(\boldsymbol{x}_1, \boldsymbol{x}_1) & \cdots & k(\boldsymbol{x}_1, \boldsymbol{x}_N) \\ \vdots & \ddots & \vdots \\ k(\boldsymbol{x}_N, \boldsymbol{x}_1) & \cdots & k(\boldsymbol{x}_N, \boldsymbol{x}_N) \end{pmatrix} \tag{3}$$

In this study, the kernel function k was obtained by the radial basis function kernel with added white noise w, as described by [36]:

$$k(\boldsymbol{x}_i, \boldsymbol{x}_j) = \theta_1 exp\left(-\frac{1}{\theta_2}|\boldsymbol{x}_i - \boldsymbol{x}_j|^2\right) + w, \tag{4}$$

where $\boldsymbol{x}_i$ and $\boldsymbol{x}_j$ are the arbitrary input points. Furthermore, θ_1 and θ_2 are hyperparameters, representing the variance and length scale, respectively. These were optimized using the limited-memory Broyden—Fletcher—Goldfarb—Shanno algorithm for bound constrained optimization [40][41]. The Python package "GPy"(version 1.9.9) [42], an open-source package to conduct GPR, was used to perform the GPR.

We used only the reconstructed altitude time series to perform Bayesian optimization and grid search, as described in the following section, because we hypothesized that the density would have a significant effect on this parameter.

2.2. Special perturbation

To estimate the density during the flight of the nanosatellites, the reconstructed trajectories were reproduced by SP, which included density as one of the inputs. The density value that

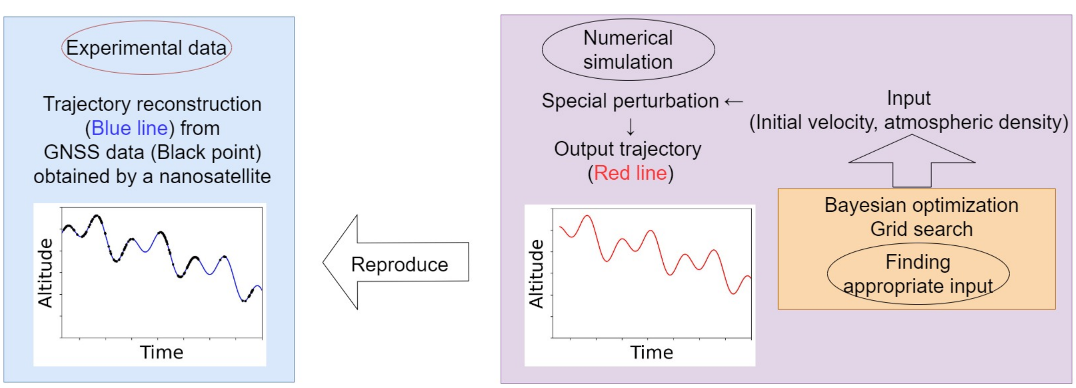

Figure 3: Concept of the methodlogy

reproduced the reconstructed trajectory was the result of this estimation. In the SP, we assumed that a nanosatellite is a point mass on an Earth-centered, Earth-fixed (ECEF) non-inertial frame. Subsequently, the Earth's gravity; Coriolis, centrifugal, and aerodynamic forces; the Sun's and Moon's gravity; tides; and solar radiation act on it. SP was calculated in this study in the region below an altitude of 250 km; therefore, the Sun's and Moon's gravity, tides and solar radiation are negligible compared to the aerodynamic force. In this case, the equation of motion was given by

$$m\frac{\partial^2 \boldsymbol{x}}{\partial t^2} = \boldsymbol{F}_{grav} - 2m\boldsymbol{\omega} \times \boldsymbol{v} - m\boldsymbol{\omega} \times (\boldsymbol{\omega} \times \boldsymbol{x}) + \boldsymbol{F}_{aero} \tag{5}$$

where $\boldsymbol{x}$, t, m, and $\boldsymbol{\omega}$ are the positioning vector, time, mass, and angular velocity vector, respectively. The velocity vector $\boldsymbol{v}$ is given by

$$\boldsymbol{v} = \frac{\partial \boldsymbol{x}}{\partial t} \tag{6}$$

The angular velocity vector represents the Earth's rotation, given by $\boldsymbol{\omega} = (0, 0, \omega)$, where $\boldsymbol{\omega} = 7.292115 \times 10^{-5}$ rad/s. Furthermore, $\boldsymbol{F}_{grav}$ and $\boldsymbol{F}_{aero}$ are the vectors for the gravitational and aerodynamic forces, respectively. $\boldsymbol{F}_{grav}$ is calculated by differentiating the gravitational potential [43]; considering the longitudinal coefficients J_{20}, J_{22}, J_{30}, and J_{40}, as obtained from the study by Liu [44], $\boldsymbol{F}_{aero}$ is given by:

$$\boldsymbol{F}_{aero} = -\frac{1}{2} d_f \rho_{model} C_D A |\boldsymbol{v}|^2 \frac{\boldsymbol{v}}{|\boldsymbol{v}|} \tag{7}$$

where d_f, ρ_{model}, C_D, and A represent the density factor, density from NRLMSISE-00, drag coefficient, and front projected area, respectively. The thermospheric horizontal wind is not considered because its effect is sufficiently low. According to the horizontal wind model HWM14 [45], the wind speed is as low as 100–150 m/s even in locally high-speed wind regions; and the wind speed distribution is symmetric with respect to a latitude of 0 degrees. Furthermore, because nanosatellites released from the ISS such as the EGG periodically move between -50 and 50 degrees latitude, the effect of the horizontal thermospheric wind can be canceled out by performing calculations over a sufficient period. Notably, this effect may not be ignored for satellites with different orbits. The date and time of the NRLMSISE-00 to calculate ρ_{model} were set to 2017/5/14, 0:00 (GMT), when the EGG was at an altitude of approximately 220 km. Furthermore, the density was calculated by averaging the global distribution ($0° \sim 360°$ longitude, in 45° increments, and $-50° \sim 50°$ latitude, in 25° increments) because the EGG stayed in this region. This means that the current SP calculation did not consider the Earth eclipse. The orbit of the EGG was almost similar to that of the ISS in terms of the longitude and latitude; it circled around the Earth in the positive direction of longitude in approximately 90 min. Therefore, the effect of the eclipse would also be canceled out in the process of obtaining the averaged orbit-derived density. The density factor was a constant value multiplied by ρ_{model}; therefore,

$$d_f = \frac{\rho_{sat}}{\rho_{model}} \tag{8}$$

where ρ_{sat} is the density experienced by the satellite. d_f value is the target of the estimation in this study. The drag coefficient of the EGG at each altitude should be accurately obtained using a wind tunnel test or computational fluid dynamics calculation using a 3D shape model of the EGG. The direct simulation Monte Carlo (DSMC) method [46] was applied as a CFD method, as described in the following subsection.

2.3. DSMC method

We used the DSMC method to calculate the C_D values of the EGG under atmospheric conditions of a high Knudsen number. The method is driven by the Boltzmann equation. The 3D shape model of the EGG and the computational grid are shown in Fig. 4. This shape was reconstructed based on the images taken in orbit by the camera (Adafruit1386) mounted on the EGG after deploying its aeroshell. We employed the Maxwellian thermal model as the wall reflection model. The wall surface was assumed to be isothermal with a temperature of 300 K, whereas the other boundary conditions were set to that of a uniform flow. The Larsen–Borgnakke model [47] was used as the collision model. In this study, the conditions were set as presented in Tables 1 and 2 at the altitude where the EGG was positioned. Here, N_{eq} represents the number of particles in a single sample. Changing N_{eq} from the values in Table 2 had almost no impact on the results of C_D. However, it affected the computational cost; hence, the values were determined so that the computational cost was acceptable. The atmospheric composition was obtained from NRLMSISE-00 on January 1, 2015, at 45° E and 55° N. OpenFOAM (ver. 4.1) [48] , an open-source CFD solver, was employed for the DSMC calculation. The solver used was "dsmcfoam". The C_D values were calculated based on the results using the equation given by

$$C_D = \frac{D}{\frac{1}{2}\rho U^2 A} \tag{9}$$

where D, ρ, U, and A are the drag force, density, velocity of flow, and front projected area of the 3D model, respectively. The yaw angle of the EGG was adjusted by 30°. The calculated C_D values are presented in Fig. 5. Although not shown, the variation of C_D to the pitch angle was almost equal to that in this figure. The C_D values were considered as cosine functions of the yaw angle, and then averaged, as shown in Fig. 6. The reason for averaging was the inability to determine the attitude of the EGG. It is hypothesized that the altitude of the EGG continued to change rapidly during the time period covered by the GNSS data used in this study (117 days after the start of the mission), as shown in Fig. 7. The C_D values ($\simeq 1.3$) shown in Fig. 6 were used for the SP with linear interpolation to the altitude.

Table 1: Conditions of the DSMC calculation commonly used for all altitudes

U (m/s)	7800
Time step (s)	10^{-5}
Number of steps	2500

Table 2: Conditions of DSMC calculation

Alt. (km)	Number density ($/m^3$) N_2	O_2	O	N	Temp. (K)	N_{eq} (-)
300	5.594e13	1.544e12	5.308e14	1.306e12	822.1	1e11
200	2.493e15	1.222e14	4.727e15	7.997e12	792.1	1e12
150	2.466e16	1.894e15	1.811e16	4.794e12	661.5	1e12

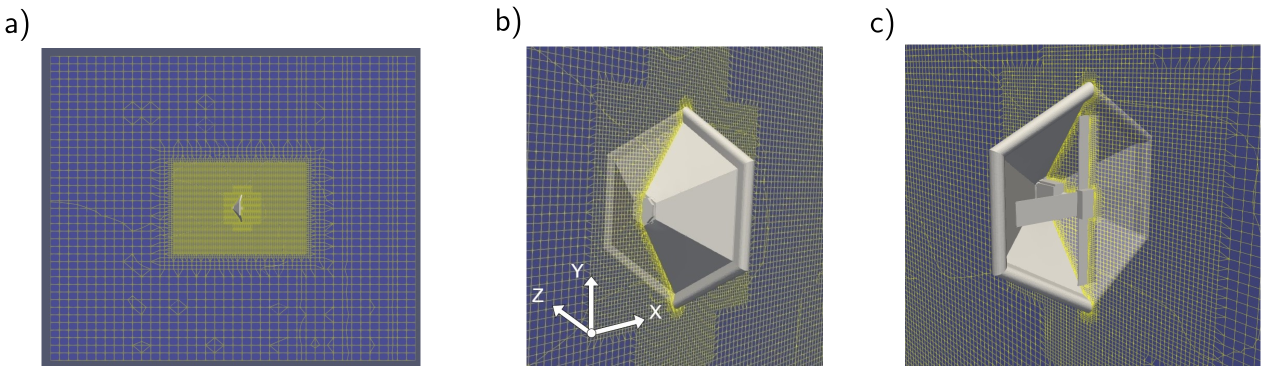

Figure 4: 3D shape model of EGG and computational grids (1,883,154 grids). (a), (b), and (c) are total computational domain, front and rear side view, respectively.

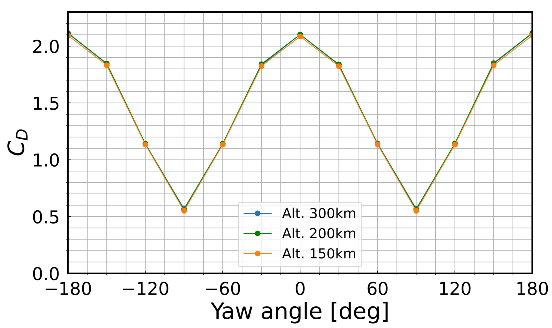

Figure 5: Results of C_D value calculation

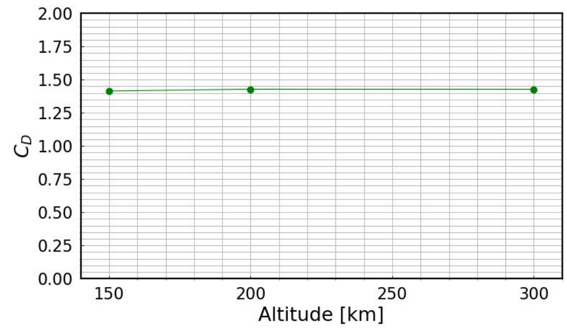

Figure 6: Averaged C_D value

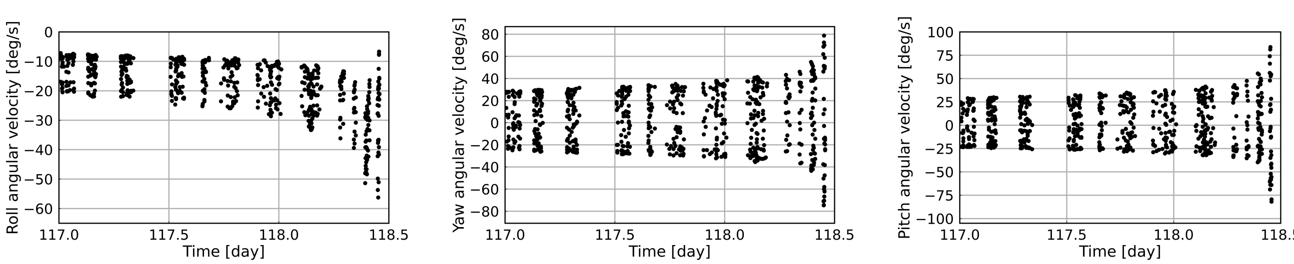

Figure 7: Angular velocity data obtained by EGG. Roll, yaw, and pitch correspond to x, y, and z in Fig. 4 (b)

2.4. Parameter search using Bayesian optimization

Eqs. (5) and (7) require several input parameters, including the density, initial velocity vector, initial coordinates, gravity potential, and physical constants such as the Earth's mass, rotation speed, and aerodynamic coefficients of the nanosatellite. The output values comprise the time-series of the coordinates and velocity. The density factor and initial velocity vector are unknown. These parameters are searched to determine the values that match the reconstructed trajectory data from GPR. BO can efficiently determine the optimal solution. The process is as follows:

1. As an initial test, random sets of input parameters (components of the initial velocity vector and density factor) are determined for the SP.
2. The selected input values are used to the SP calculations and the trajectory data are obtained.
3. The objective function, the difference between these and the reconstructed trajectory, is calculated using Eq. 10.
4. Utilizing the results used to train the data, GPR is used to create a predictive distribution of the objective function in the input parameter space.
5. The pair of input parameters for the predictive distribution of the objective function is minimized and estimated by the acquisition function.
6. Steps 2 through 5 are iterated until umbral is established; the input parameters resulting in the smallest objective function are regarded as the optimization results.

The objective function f minimized by BO was defined as

$$\begin{aligned} f =& \frac{1}{N} \sum_{i}^{N} \left(\frac{|\boldsymbol{x}_{i,alt,GPR} - \boldsymbol{x}_{i,alt,SP}|}{\boldsymbol{x}_{i,alt,GPR}} \right) \\ &+ \frac{|t_{set,GPR} - t_{set,SP}|}{t_{set,GPR}} \times w_t \end{aligned} \tag{10}$$

where $\boldsymbol{x}$ and t represent the coordinates and time, respectively, with subscripts GPR and SP indicating the error evaluation points for GPR and SP, respectively. The term N represents the number of error evaluation points, and i represents each point. The first term on the right side of the equation represents the average altitude difference rate at each point. The second term is the difference in time when the altitude reaches the set value, and w_t is a weight parameter to account for the earliness of the drop. The Matern 5/2 kernel [49] was used for the BO. The expected improvement [50] was used as the acquisition function. The Python package "GPyOpt" (ver.1.2.6) [51], an open-source package to conduct BO, was used to perform BO. The model was set as a standard Gaussian process (GP).

Focusing on the low cost of BO, we repeated the process of "random initial test → maximum number of iterations reached" 100 times and obtained 100 patterns of the optimization results. These were approximately optimal values; therefore, a more detailed grid search was performed, as described in the following subsection.

2.5. Detailed grid search

A grid search is a parameter search method that sets the range and resolution of the input parameters and searches all patterns. With this approach, we can estimate the optimal input parameters, minimizing the difference in altitude, and analyze their sensitivities near the optimal value. In this study, the following steps were performed for all cases: selection of the input parameters of SP and calculation of the difference from the reconstructed trajectory.

3. Trajectory reconstruction by GPR

We reconstructed the trajectory of the EGG using GNSS data before the end of the mission, specifically, before atmospheric re-entry as shown in Fig. 2 (c). The initial values of the hyperparameters and the number of iterations for the optimization of the kernel function shown in Eq. 4 were 1 and 1000 for θs and max iteration, respectively. Fig. 8 shows the results of the trajectory reconstruction using GPR. GPR provides the mean and variance of the predictive Gaussian distribution. The blue lines represent the mean of the predictive distribution, whereas the light blue bands indicate the 95% confidence range; however, they are almost invisible because the maximum values of these ranges were approximately 200 m, which was sufficiently low. They were sufficiently accurate for the density estimations.

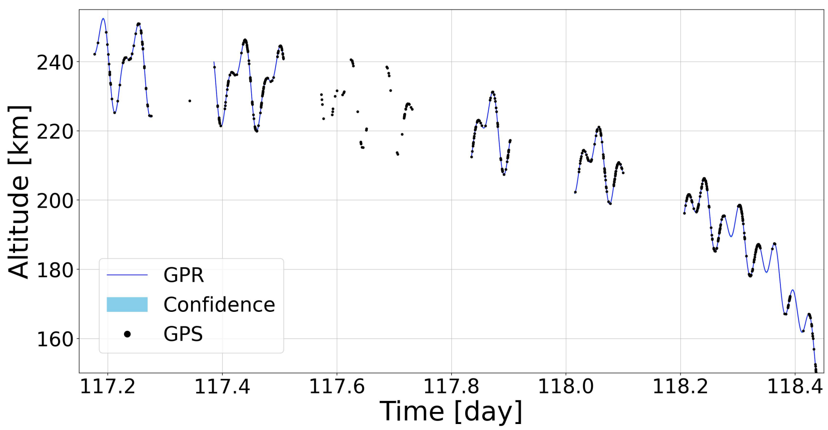

Figure 8: Results of Gaussian process regression

4. Density prediction performance

A validation test was conducted as follows:

1. Virtual ground-truth trajectory data were generated using the SP with a specific set of input parameters (initial velocity vector $\boldsymbol{v}_{I,true}$ and density factor $d_{f,true}$).
2. The reconstructed trajectory from the GNSS data, located in the lower left of Fig. 3, was replaced with the ground-truth data. The initial velocity vector and density factor were optimized using BO within certain ranges including their ground-true values. BO was performed for 100 sets, as described in Section 2.4.
3. The ranges of the input parameters for the detailed grid search were determined from the 100 patterns of the BO results.
4. A grid search was performed to determine the condition that minimized the altitude difference between the ground-truth trajectory data and the output of the SP, and verify whether this condition was equal to $\boldsymbol{v}_{I,true}$ and $d_{f,true}$. The sensitivity of each parameter was also discussed.

4.1. Ground-truth data

SP was performed under the conditions listed in Table 3 to obtain the ground-truth data, as shown in Fig. 9. In Table 3, $\boldsymbol{x}_{I,true} = (x_{I,long,true}, x_{I,lati,true}, x_{I,alti,true})$, $\boldsymbol{v}_{I,true} = (v_{I,long,true}, v_{I,lati,true}, v_{I,alti,true})$, and $d_{f,true}$ are the initial coordinates, velocity vector, and density factor, respectively.

Table 3: Parameters for ground-truth data

Parameters	Values
$\mathrm{x_{I,long,true}}$ (deg)	-145
$\mathrm{x_{I,lati,true}}$ (deg)	50
$\mathrm{x_{I,alti,true}}$ (deg)	210
$\mathrm{v_{I,long,true}}$ (m/s)	7200
$\mathrm{v_{I,lati,true}}$ (m/s)	-2070
$\mathrm{v_{I,alti,true}}$ (m/s)	15
$\mathrm{d_{f,true}}$	1.0

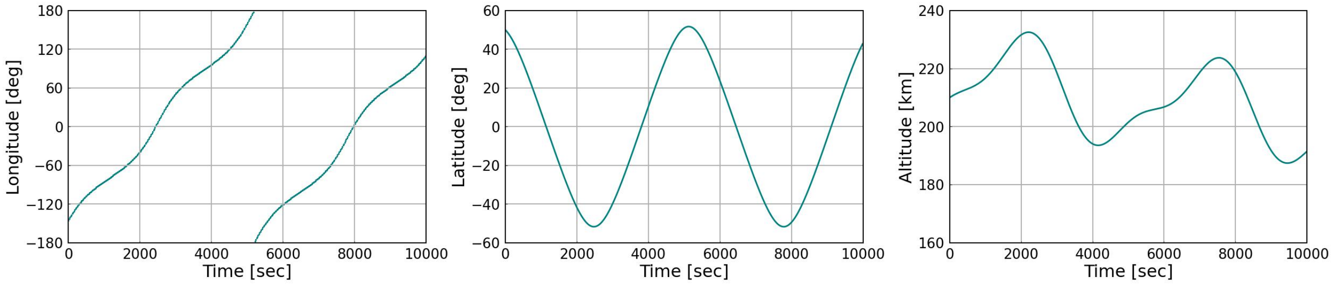

Figure 9: Ground-truth data

4.2. Bayesian optimization against ground-truth data

BO was performed 100 times under the conditions listed in Table 4. The "set altitude" indicates the altitude at which the time difference in Eq. 10 was calculated. The total computational time (wall time) was approximately 2 h. Among the obtained 100 patterns of the optimization results ($V_{I,opt} = (\boldsymbol{v}_{I,opt,1}, ..., \boldsymbol{v}_{I,opt,100})$, $D_{f,opt} = (d_{f,opt,1}, ..., d_{f,opt,100})$),the best results ($\boldsymbol{v}_{I,opt,best}$, $d_{f,opt,best}$) closest to the altitude ground-truth data, the trajectory (red line), and the error magnitude (pink line) are shown in Fig. 10. The red line is almost invisible because the maximum values of the error was approximately 0.5 km. The closeness of the two-trajectory data was evaluated using the average difference in altitude at each point ($Err_{alt,ave}$). This figure shows that the initial velocity vector and density factor, which were close to the ground-truth data, were obtained by the BO. Furthermore, it shows that the $d_{f,opt,best} = 0.944$ is close to the $d_{f,true} = 1.0$ in Table 3. Fig. 11 shows the distributions of $Err_{alt,ave}$ for each input parameter $V_{I,long,opt}$, $V_{I,lati,opt}$, $V_{I,alti,opt}$, $V_{I,opt}$'s longitude, latitude, and altitude components, respectively, and $D_{f,opt}$. The distribution of the magnitude values of $V_{I,opt}$, $V_{I,mag,opt}$ is also shown in Fig. 11 (e). This value was not an input parameter but was calculated by

$$\sqrt{v_{I,long,opt,j}^2 + v_{I,lati,opt,j}^2} \approx v_{I,mag,opt,j}, \tag{11}$$

because,

$$v_{I,alti,opt,j} \ll v_{I,long,opt,j}, v_{I,lati,opt,j} \tag{12}$$

Fig. 11 (c), (d), and (e) show that $V_{I,alti,opt}$, $D_{f,opt}$, and $V_{I,mag,opt}$, have downward convex distributions centered on $v_{I,alti,true}$, and $d_{f,true}$, in Table 3, and $v_{I,mag,true}$, in Fig. 11 (e), respectively. They show that these parameters gathered toward these ground-truth values. This may be because of the preferential search by the BO, because they have a impact on the altitude of the trajectory. It can also be inferred that BO revealed parameters that have a impact on the altitude.

Table 4: Settings for Bayesian optimization (validation)

Parameters	Values
$V_{I,long,bopt}$ (m/s)	[7150, 7250]
$V_{I,lati,bopt}$ (m/s)	[-2120, -2020]
$V_{I,alti,bopt}$ (m/s)	[0, 20]
$D_{f,bopt}$	[0, 2]
Set altitude (km)	190
Weight of time, w_t	1e-6
Number of initial tests	5
Max iterations	300

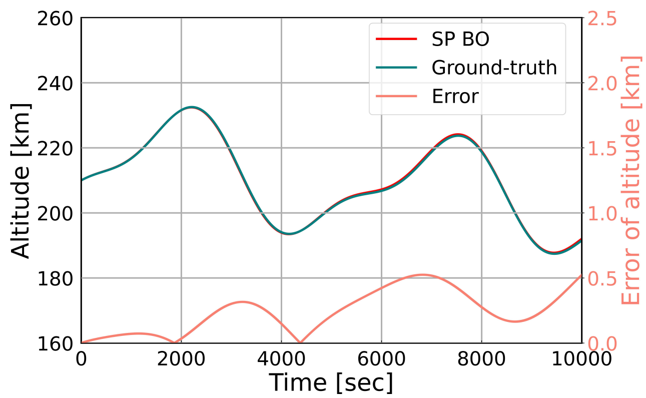

Figure 10: Closest result of trajectory reproduction by BO. $v_{I,opt,best} = (7187.6, -2114.1, 15.3)$ (m/s), $d_{f,opt,best} = 0.944$

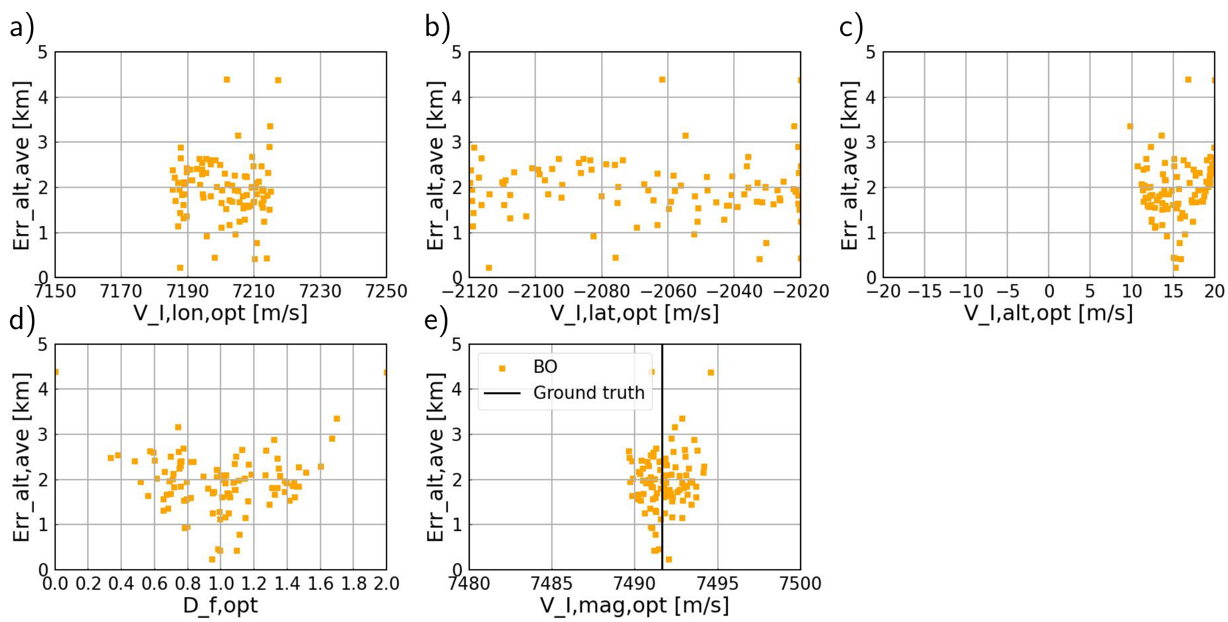

Figure 11: Distributions of the optimized parameters (prediction performance)

4.3. Grid searching against the ground-truth data

The ranges of the input parameters for the grid search were determined based on the BO results, as listed in Table 6. The list of variations for each input parameter was named $V_{I,long,grid}$, $V_{I,lati,grid}$, and $V_{I,alti,grid}$, respectively. Based on the results in Fig. 11 (e), we assumed that the magnitude of the initial velocity vector could be used as a constraint to reduce the computational cost. $v_{I,mag,min}$ and $v_{I,mag,max}$ were the constraints. Thus, we conducted SP only when $v_{I,long,grid,j}$ and $v_{I,lati,grid,k}$ satisfied the constraint as given by

$$v_{I,mag,min} < \sqrt{v_{I,long,grid,j}^2 + v_{I,lati,grid,k}^2} < v_{I,mag,max}. \tag{13}$$

They were given as the maximum integer value that does not exceed the minimum value of $V_{I,mag,opt}$ and the minimum integer value that exceeds the maximum value. A grid search was conducted using the conditions listed in Table 5. The total number of cases was 86,660. The number of cases without the constraints in Eq. 13 was 452,480, thereby reducing the number of calculations to approximately one-fifth. Fig. 12 shows the results with $Err_{alt,ave}$ ($\leq$ 2 km) on the vertical axis and each input parameter on the horizontal axis, similar to Fig. 11. First, Fig. 12 (a) and (b) show that the values of $V_{I,long,grid}$ and $V_{I,lati,grid}$ have no effect on $Err_{alt,ave}$. In other words, even if these two parameters have different values from $v_{I,long,true}$, $Err_{alt,ave}$ becomes extremely small depending on the other parameters. Therefore, these two parameters could not be estimated based on the smallness of $Err_{alt,ave}$. Fig. 12 (c), (d), and (e) show that $V_{I,alti,grid}$, $D_{f,grid}$, and $V_{I,mag,grid}$ have a certain effect on $Err_{alt,ave}$ because the distributions of this value became convex downward with $v_{I,alti,true}$, $d_{f,true}$, and $v_{I,mag,true}$ at the center, similar to the case of BO. Therefore, it was shown that these parameters could be estimated by performing a BO and grid search. Furthermore, it was possible to estimate these parameters in the case of EGG using the reconstructed trajectory from the EGG GNSS data shown in Fig. 8. Compared with the methodology using high-precision and high-temporal GNSS data, for example [9], the proposed methodology is advantageous in terms of the measurement costs. Usually, satellite missions are expensive; however, using our methodology, the information on the density in the VLEO can be obtained from low-cost nanosatellites intermittent data. Finally, the sensitivities of these parameters to $Err_{alt,ave}$ were interpreted from the results. Focusing on d_f, which is the target of this study, Fig. 12 (d) shows that $Err_{alt,ave}$ changes by approximately 0.5 km with a change of 0.15 in $D_{f,grid}$. This can be used to determine the estimation error of d_f. For example, considering the GNSS measurement error, if the acceptable maximum error of $Err_{alt,ave}$ is determined as 0.5 km, the estimation error of the density is determined as approximately $\pm$ 0.15 in this case. Compared with [9], this is a drawback in terms of the spatial and temporal resolution. The sensitivity of d_f to $Err_{alt,ave}$ depends on the length of time taken for the SP calculation because the longer the time, the larger the perturbation. Therefore, a certain time span is necessary to obtain density from our methodology; this is the averaged value along a certain trajectory length.

5. Atmospheric density in VLEO

The altitude intervals (A)–(D) shown in Fig. 13 were set based on the reconstructed trajectory of the EGG shown in Fig. 8. For each of these intervals, BO and grid search were performed as in Section 5 to estimate d_f. As described in Section 4, BO was performed 100 times under the conditions listed in Table 6. The ranges of $V_{I,long,bopt}$ and $V_{I,lati,bopt}$ were determined experimentally such that the magnitudes of the velocities converged, as shown in Fig. 11 (e), based on the results of the GPR on the longitude and latitude GNSS data. This was because the velocity of EGG could

Table 5: Ranges of parameters for grid search (validation)

Parameters	Values	Resolution
$V_{I,long,grid}$ (m/s)	[7184, 7218]	2
$V_{I,lati,grid}$ (m/s)	[-2120, -2020]	2
$V_{I,alti,grid}$ (m/s)	[12, 18]	2
$D_{f,grid}$	[0.75, 1.25]	0.05
$v_{I,mag,min}/v_{I,mag,max}$	7489/7495	#

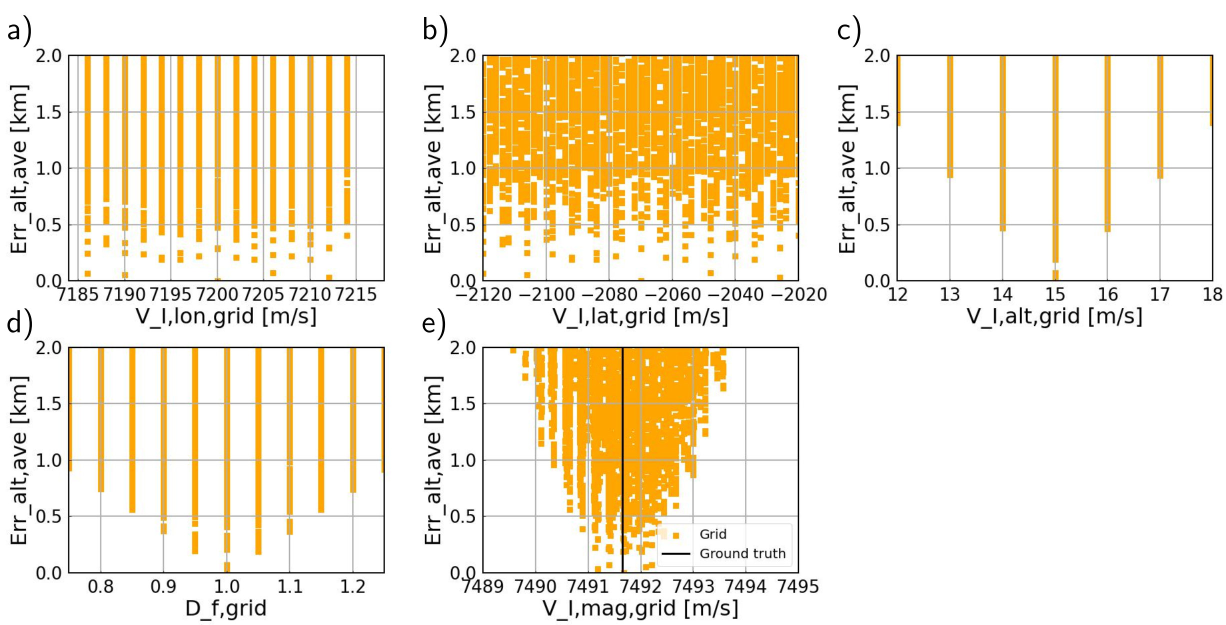

Figure 12: Distributions of the grid search results (prediction performance)

not be reconstructed accurately, according to [36]. As an example, the BO results for interval (A) are shown in Fig.14 as well as Fig. 11. The distribution of each input parameter was almost identical to that used in the validation. The results for the other intervals were similar. Based on these results, the grid search conditions were set as listed in Table 7.

Additionally, the results of the grid search for interval (A) are shown in Fig. 15 as well as Fig. 12, and are almost similar to the validation results. The results for the other intervals were similar. In other words, we could capture the range of optimal values for the altitude component and magnitude value of the initial velocity vector, as well as the density factor using BO. This enabled an effective grid search.

Fig. 16 shows d_f distribution, as shown in Fig. 11 (d). In each interval, the minimum $Err_{alt,ave}$ were 0.07 km, 0.12 km, 0.07 km, and 0.18 km, respectively. The d_f values in each interval, which output the minimum $Err_{alt,ave}$, were 0.50, 0.56, 0.58, and 0.64, respectively. From Eq. 8, the density EGG experienced (ρ_{EGG}) was

$$\rho_{EGG} = d_f \rho_{model}. \tag{14}$$

Thus, in each interval, ρ_{EGG} was estimated as 0.50, 0.56, 0.58, and 0.64 times greater than that of the NRLMSISE-00, respectively. This suggests that the model may overestimate the density at an altitude of approximately 200 km. However, the EGG does not have attitude data and we used averaged C_D values in SP, as mentioned in Section 2.3. To perform more accurate validation on the atmospheric model, we should use GNSS data obtained by nanosatellites, which obtain attitude data within the same time as BEAK [52], the successor of EGG, which began flight demonstrations on December 18, 2023. Data obtained from the spherical satellites can be used for this purpose. Performing spherical nanosatellite missions to estimate the density of the VLEO is particularly effective. In addition, the modeling of the SP calculations described in Section 2.2 has a certain effect on accuracy. For example, the ρ_{model} is the altitude distribution averaged over the longitude and latitude in the region where the EGG rested and is stationary. In reality, the density varies with the Earth's eclipses and time. More accurate density estimation will be possible by taking into account such changes in the atmospheric density during SP calculation. Moreover, the parameter used here to estimate the density is d_f; however, a more meaningful estimate would be obtained using a parameter that is more consistent with the structure of the thermospheric density, such as $F10.7$.

Furthermore, Fig. 16 shows that the slopes of the distributions are different with the interval. As mentioned in Section 4.3, these slopes show the sensitivity of d_f to $Err_{alt,ave}$; they depend on the length of time. Comparing interval (A) and (D), the trajectory of (D) is shorter (Fig. 13) but its slope is steeper. This may be because of the higher density at lower altitudes and the greater effect on the trajectory altitude by the percentage change in the density. From these results, it can be deduced that our methodology visualizes the sensitivity of d_f to $Err_{alt,ave}$, corresponding to the time length and altitude of the GNSS data we used as well as the reconstructed trajectory. As mentioned in Section 4.3, determining the maximum allowable $Err_{alt,ave}$ is a significant issue. If this value can be determined by appropriately considering the errors in the GNSS data, the methodology developed in this study can be used to estimate the density factor and its range.

6. Conclusion

In this study, we developed a methodology for estimating atmospheric density based on intermittent GNSS data collected from nanosatellites. This approach corrects the density predicted by the NRLMSISE-00 model in the process of reproducing the predicted trajectory from the GNSS

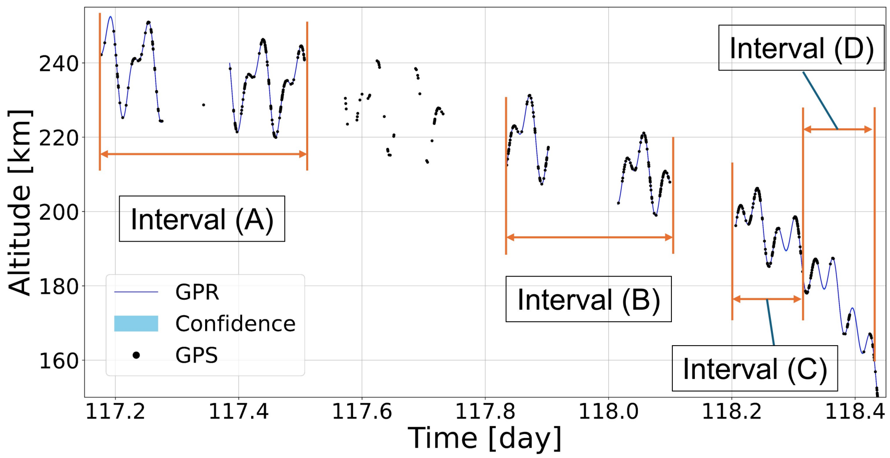

Figure 13: Intervals to estimate density

Table 6: Settings for Bayesian optimization (EGG data)

Parameters	Values			
Intervals	A	B	C	D
$V_{I,long,bopt}$ (m/s)	[6100, 6200]	[6000, 6100]	[7150, 7250]	[4400, 4450]
$V_{I,lati,bopt}$ (m/s)	[4150, 4250]	[4350, 4450]	[-2150, -2050]	[6050, 6150]
$V_{I,alti,bopt}$ (m/s)	[-20, 20]			
$D_{f,bopt}$	[0, 2]			
Weight of time, w_t	1e-3			
Set altitude (km)	220	200	180	160
Number of initial tests	5			
Max iteration	300			

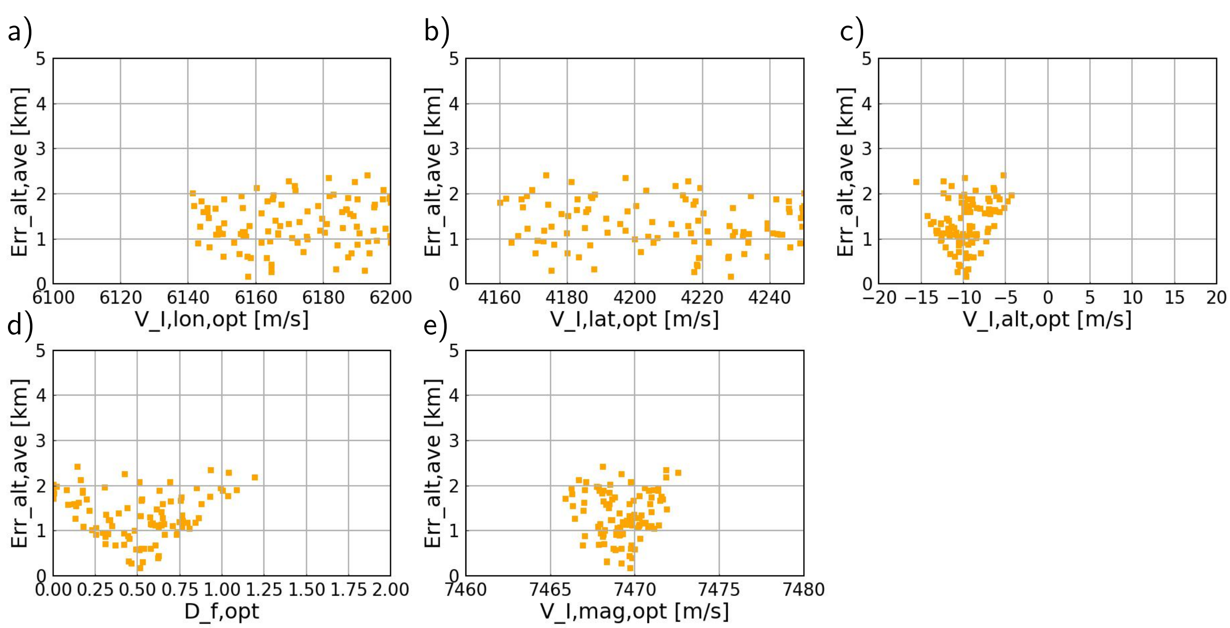

Figure 14: Distributions of the optimized parameters (EGG data, Interval (A))

Table 7: Ranges of parameters for grid search (EGG data)

Parameters	Values				Resolutions
Intervals	A	B	C	D	
$V_{I,long,grid}$ (m/s)	[6140, 6200]	[6020, 6100]	[7178, 7210]	[4400, 4450]	2
$V_{I,lati,grid}$ (m/s)	[4160, 4250]	[4350, 4450]	[-2150, -2050]	[6050, 6150]	2
$V_{I,alti,grid}$ (m/s)	[-13, -7]	[-3, 3]	[4, 8]	[-7, 0]	2
$D_{f,grid}$	[0.2, 0.8]	[0.3, 0.74]	[0.4, 0.8]	[0.48, 0.8]	0.02
$v_{I,mag,min}/v_{I,mag,min}$	7465/7472	7483/ 7493	7489/7500	7505/7532	#

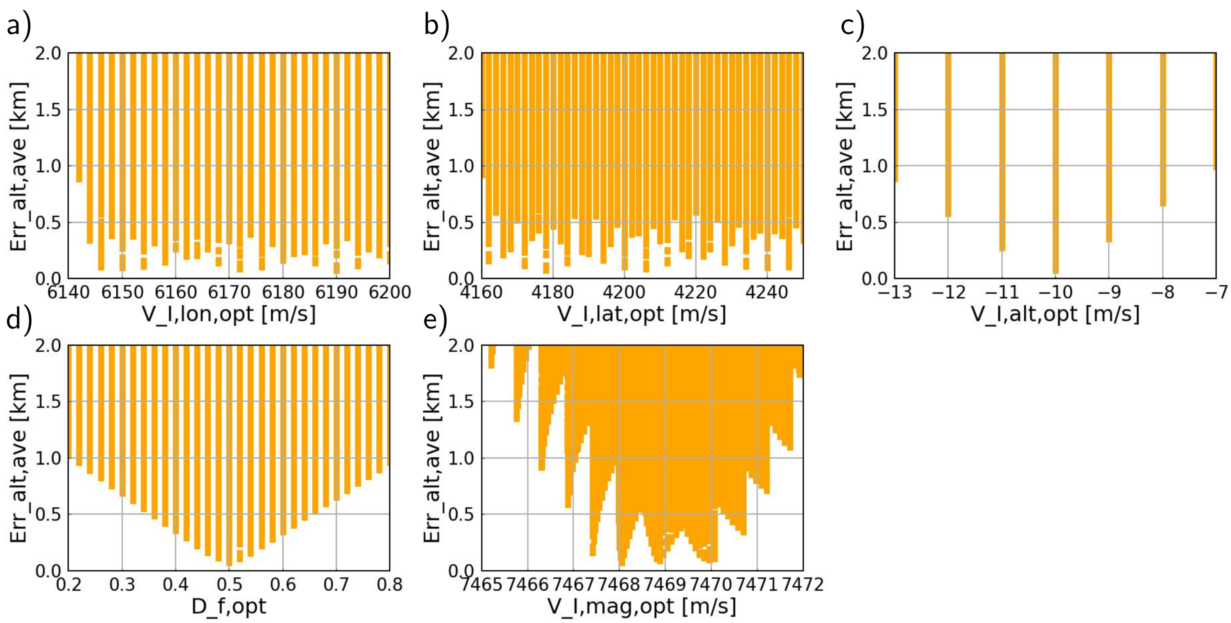

Figure 15: Distributions of the grid search results (EGG data, interval (A))

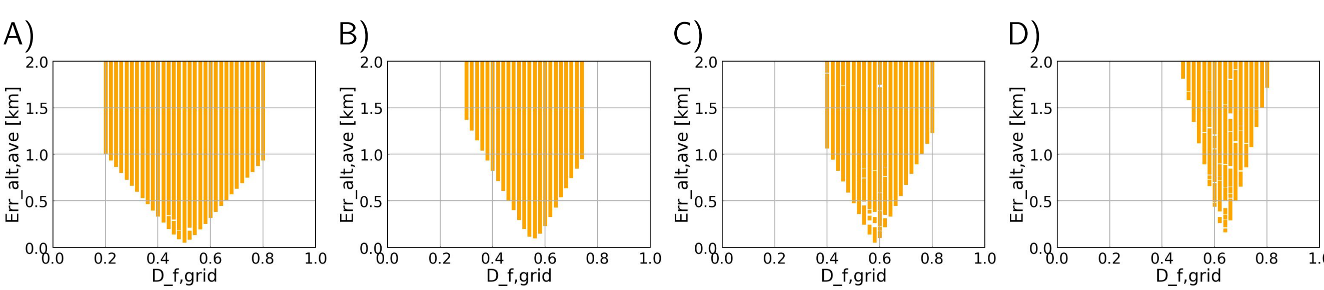

Figure 16: Distributions of the grid search EGG data results, only density factor (EGG data). (A)–(D) are the names of intervals.

data by special perturbation. We validated the methodology using virtual ground-truth data and applied it to the measured GNSS data from the nanosatellite EGG.

First, trajectories were reconstructed from the intermittent GNSS data measured by the EGG using GPR. The results were sufficiently accurate for density estimation.

Subsequently, the methodology developed in this study was validated. The virtual ground-truth data were created using SP to simulate the EGG trajectory. The methodology was validated by optimizing the components of the initial velocity vector and density factor using BO and grid search. The results indicated that the density factor and its estimation error could be estimated. Subsequently, the advantages and drawbacks with respect to the methodology based on the high temporal GNSS data were discussed.

Finally, the methodology was applied to the EGG data, and the initial velocity component and density factor that matched the reconstructed trajectory were obtained. The results suggest that the empirical atmospheric model NRLMSISE-00 may overestimate the density at altitudes around 200 km. Furthermore, we successfully visualized the sensitivity of the density corresponding to the time length and altitude of the GNSS data we used and reconstructed their trajectory. The limitations and future work for further development of the methodology were discussed.

Declaration of competing interest

The authors declare that they have no known competing financial interests or personal relationships that could have appeared to influence the work reported in this paper.

Declaration of Generative AI and AI-assisted technologies in the writing proces

During the preparation of this work the authors used DeepL and Grammarly in order to improve readability and language. After using these tools, the authors reviewed and edited the content as needed and take full responsibility for the content of the publication.

Acknowledgments

The EGG mission was realized using KIBO, the Japanese experimental module of ISS and affords unique functions including an airlock and a robotic arm as well as the opportunity to use the J-SSOD system provided by the JEM Mission Operation and Integration Center, Human Spaceflight Technology Directorate, JAXA. This work was supported by JSPS KAKENHI Grant Number 23H00212. The computations were performed using the intercloud system at the information initiative center, Hokkaido University and the computational facilities at the Research Institute for Information Technology, Kyushu University.

References

[1] J.T. Emmert. Thermospheric mass density: A review. Advances in Space Research, 56(5):773–824, September 2015.

[2] Shuanggen Jin, Andres Calabia, and Liangliang Yuan. Thermospheric Variations From GNSS and Accelerometer Measurements on Small Satellites. Proc. IEEE, 106(3):484–495, March 2018.

[3] J. M. Picone, J. T. Emmert, and J. L. Lean. Thermospheric densities derived from spacecraft orbits: Accurate processing of two-line element sets. J. Geophys. Res., 110(A3):2004JA010585, March 2005.

[4] Bruce R Bowman, Frank A Marcos, and Michael J Kendra. A method for computing accurate daily atmosphere density velues from satellite drag data. 14th AAS/AIAA Space Flight Mechanics Conference, 119:1117–1134, 2004.

[5] S. Bruinsma, D. Tamagnan, and R. Biancale. Atmospheric densities derived from CHAMP/STAR accelerometer observations. Planetary and Space Science, 52(4):297–312, March 2004.

[6] Eric K. Sutton, R. Steven Nerem, and Jeffrey M. Forbes. Density and Winds in the Thermosphere Deduced from Accelerometer Data. Journal of Spacecraft and Rockets, 44(6):1210–1219, November 2007.

[7] Andres Calabia and Shuanggen Jin. New modes and mechanisms of thermospheric mass density variations from GRACE accelerometers. JGR Space Physics, 121(11), November 2016.

[8] Andres Calabia and Shuanggen Jin. Thermospheric density estimation and responses to the March 2013 geomagnetic storm from GRACE GPS-determined precise orbits. Journal of Atmospheric and Solar-Terrestrial Physics, 154:167–179, February 2017.

[9] Andrés Calabia and Shuanggen Jin. Upper-Atmosphere Mass Density Variations From CASSIOPE Precise Orbits. Space Weather, 19(4):e2020SW002645, April 2021.

[10] C. Arduini, G. Laneve, and F. A. Herrero. Local time and altitude variation of equatorial thermosphere midnight density maximum (MDM): San Marco drag balance measurements. Geophysical Research Letters, 24(4):377–380, February 1997.

[11] F. Santoni, F. Piergentili, and F. Graziani. Broglio Drag Balance for neutral thermosphere density measurement on UNICubeSAT. Advances in Space Research, 45(5):651–660, March 2010.

[12] A. E. Hedin. Msis-86 thermospheric model. J. Geophys. Res., 92(A5):4649–4662, 1987.

[13] R. R. Meier, J. M. Picone, D. Drob, J. Bishop, J. T. Emmert, J. L. Lean, A. W. Stephan, D. J. Strickland, A. B. Christensen, L. J. Paxton, D. Morrison, H. Kil, B. Wolven, Thomas N. Woods, G. Crowley, and S. T. Gibson. Remote Sensing of Earth's Limb by TIMED/GUVI: Retrieval of thermospheric composition and temperature. Earth and Space Science, 2(1):1–37, January 2015.

[14] R. R. Meier and J. M. Picone. Retrieval of absolute thermospheric concentrations from the far UV dayglow: An application of discrete inverse theory. J. Geophys. Res., 99(A4):6307–6320, April 1994.

[15] J. H. Clemmons, J. H. Hecht, D. R. Salem, and D. J. Strickland. Thermospheric density in the Earth's magnetic cusp as observed by the Streak mission. Geophysical Research Letters, 35(24):2008GL035972, December 2008.

[16] P. Bauer, P. Waldteufel, and D. Alcayde. Diurnal variations of the atomic oxygen density and temperature determined from incoherent scatter measurements in the ionospheric F region. J. Geophys. Res., 75(25):4825–4832, September 1970.

[17] M. J. Buonsanto, Y. -K. Tung, and D. P. Sipler. Neutral atomic oxygen density from nighttime radar and optical wind measurements at Millstone Hill. J. Geophys. Res., 97(A6):8673–8679, June 1992.

[18] A. C. Aikin, A. E. Hedin, D. J. Kendig, and S. Drake. Thermospheric molecular oxygen measurements using the ultraviolet spectrometer on the Solar Maximum Mission Spacecraft. J. Geophys. Res., 98(A10):17607–17613, October 1993.

[19] Jon R. Determan, Scott A. Budzien, Michael P. Kowalski, Michael N. Lovellette, Paul S. Ray, Michael T. Wolff, Kent S. Wood, Lev Titarchuk, and Reba Bandyopadhyay. Measuring atmospheric density with X-ray occultation sounding. J. Geophys. Res., 112(A6):2006JA012014, June 2007.

[20] A. E. Hedin, J. E. Salah, J. V. Evans, C. A. Reber, G. P. Newton, N. W. Spencer, D. C. Kayser, D. Alcaydè, P. Baue, L Cogger, and J. P. McClure. A global thermospheric model based on mass spectrometer and incoherent scatter data msis, 1. n2 density and temperature. J. Geophys. Res., 82:2139–2147, 1977.

[21] A. E. Hedin, C. A. Reber, G. P. Newton, N. W. Spencer, H. C. Brinton, H G Mayr, and W. E. Potter. A global thermospheric model based on mass spectrometer and incoherent scatter data msis. 2. composition. J. Geophys. Res., 82:2148–2156, 1977.

[22] A. E. Hedin. A revised thermospheric model based on mass spectrometer and incoherent scatter data: Msis-83. J. Geophys. Res., 82:10170–10188, 1983.

[23] A. E. Hedin. Extension of the msis thermosphere model into the middle and lower atmosphere. J. Geophys. Res., 96(A2):1159–1172, 1991.

[24] J. M. Picone, A. E. Hedin, D. P. Drob, and A. C. Aikin. NRLMSISE-00 empirical model of the atmosphere: Statistical comparisons and scientific issues. J. Geophys. Res., 107(A12), December 2002.

[25] J. T. Emmert, D. P. Drob, J. M. Picone, D. E. Siskind, M. Jones, M. G. Mlynczak, P. F. Bernath, X. Chu, E. Doornbos, B. Funke, L. P. Goncharenko, M. E. Hervig, M. J. Schwartz, P. E. Sheese, F. Vargas, B. P. Williams, and T. Yuan. NRLMSIS 2.0: A Whole-Atmosphere Empirical Model of Temperature and Neutral Species Densities. Earth and Space Science, 8(3):e2020EA001321, March 2021.

[26] F. Barlier, C. Berger, J. L. Falin, G. Kockaers, and G. Thuillier. A thermospheric model based on satellite drag data. J. Geophys. Res., 34:2–24, 1978.

[27] C. Berger, R. Biancale, F. Barlier, and M. Ill. Improvement of the empirical thermospheric model DTM: DTM94 - a comparative review of various temporal variations and prospects in space geodesy applications. Journal of Geodesy, 72(3):161–178, March 1998.

[28] S. Bruinsma, G. Thuillier, and F. Barlier. The DTM-2000 empirical thermosphere model with new data assimilation and constraints at lower boundary: accuracy and properties. Journal of Atmospheric and Solar-Terrestrial Physics, 65(9):1053–1070, June 2003.

[29] Sean Bruinsma. The DTM-2013 thermosphere model. J. Space Weather Space Clim., 5:A1, 2015.

[30] L. G. Jacchia. Static diffusion models of upper atmosphere with empirical temperature profiles. Smithsonian Contr. Astrophys., 8:215–257, 1965.

[31] L. G. Jacchia. New static models of the thermosphere and exosphere with empirical temperature profiles. Smithson. Astrophys. Obs. Spec. Rep., 313:1–113, 1970.

[32] L. G. Jacchia. Revised static models of the thermosphere and exosphere with empirical temperature profiles. Smithson. Astrophys. Obs. Spec. Rep., 332, 1971.

[33] Mark F. Storz, Bruce R. Bowman, Major James I. Branson, Stephen J. Casali, and W. Kent Tobiska. High accuracy satellite drag model (HASDM). Advances in Space Research, 36(12):2497–2505, January 2005.

[34] Bruce R. Bowman, W. Kent Tobiska, Frank A. Marcos, and Cesar Valladares. The JB2006 empirical thermospheric density model. Journal of Atmospheric and Solar-Terrestrial Physics, 70(5):774–793, March 2008.

[35] David Vallado, Paul Crawford, Ricahrd Hujsak, and T.S. Kelso. Revisiting Spacetrack Report #3. In AIAA/AAS Astrodynamics Specialist Conference and Exhibit, Keystone, Colorado, August 2006. American Institute of Aeronautics and Astronautics.

[36] Yusuke Takahashi, Masahiro Saito, Nobuyuki Oshima, and Kazuhiko Yamada. Trajectory reconstruction for nanosatellite in very low Earth orbit using machine learning. Acta Astronautica, 194:301–308, May 2022.

[37] Iridium short burst data(sbd). `https://www.iridium.com/services/iridium-sbd/`, Accessed 2023/1/31.

[38] Carl Edward Rasmussen and Christopher K. I. Williams. Gaussian processes for machine learning. Adaptive computation and machine learning. MIT Press, Cambridge, Mass, 2006. OCLC: ocm61285753.

[39] Eric Brochu, Vlad M. Cora, and Nando de Freitas. A Tutorial on Bayesian Optimization of Expensive Cost Functions, with Application to Active User Modeling and Hierarchical Reinforcement Learning. December 2010. arXiv:1012.2599 [cs].

[40] Richard H Byrd, Peihuang Lu, Jorge Nocedal, and Ciyou Zhu. A LIMITED MEMORY ALGORITHM FOR BOUND CONSTRAINED OPTIMIZATION. 16(5):1190–1208, 1995.

[41] Ciyou Zhu, Richard H. Byrd, Peihuang Lu, and Jorge Nocedal. Algorithm 778: L-BFGS-B: Fortran subroutines for large-scale bound-constrained optimization. ACM Transactions on Mathematical Software, 23(4):550–560, December 1997.

[42] Gpy - a gaussian process (gp) framework in python. `https://gpy.readthedocs.io/en/deploy/`, Accessed 2023/1/31.

[43] C A Wagner. THE GRAVITY POTENTIAL AND FORCE FIELD OFTHEEARTHTHROUGHFOURTHORDER. NASA TN, D-3317:1–60, 1971.

[44] Fucheng. Liu, Shan. Lu, and SpringerLink (Online service). Guidance and Control Technology of Spacecraft on Elliptical Orbit. Navigation: Science and Technology,. Springer Singapore :, Singapore :, 1st ed. 2019. edition, 2019.

[45] Douglas P. Drob, John T. Emmert, John W. Meriwether, Jonathan J. Makela, Eelco Doornbos, Mark Conde, Gonzalo Hernandez, John Noto, Katherine A. Zawdie, Sarah E. McDonald, Joe D. Huba, and Jeff H. Klenzing. An update to the Horizontal Wind Model (HWM): The quiet time thermosphere. Earth and Space Science, 2(7):301–319, July 2015.

[46] G.A. Bird. Molecular Gas Dynamics and the Direct Simulation of Gas Flows. Number 1 in Molecular Gas Dynamics and the Direct Simulation of Gas Flows. Clarendon Press, 1994.

[47] Claus Borgnakke and Poul S. Larsen. Statistical collision model for Monte Carlo simulation of polyatomic gas mixture. Journal of Computational Physics, 18(4):405–420, August 1975.

[48] Openfoam the open source cfd toolbox. ESI-OpenCFD, `http://www.openfoam.com/`, Accessed 2023/1/31.

[49] Milton Abramowitz and Irene A. Stegun. Handbook of Mathematical Functions with Formulas, Graphs, and Mathematical Tables. Dover, New York, ninth dover printing, tenth gpo printing edition, 1964.

[50] J. Mockus, Vytautas Tiesis, and Antanas Zilinskas. The application of Bayesian methods for seeking the extremum, volume 2, pages 117–129. 09 2014.

[51] Gpyopt's documentation. `https://gpyopt.readthedocs.io/en/latest/`, Accessed 2023/1/31.

[52] Y. Nagata, T. Moriyoshi, K. Yamada, F. Akiyama, T. Ota, T. Miyamori, K. Matsuo, H. Ueshima, Imamura O. and Shoji Y. Fujiwara, M. and, D. Akita, and Suzuki K. Watanabe, Y. and. Development and flight plan of nanosatellite beak for breakthrough technology demonstration using deployable aeroshell. International Conference on Flight Vehicles, Aerothermodynamics and Re-entry Missions and Engineering (FAR), 2022.